Journal of Power Sources 398 (2018) 67–74

Contents lists available at ScienceDirect

Journal of Power Sources

journal homepage: www.elsevier.com/locate/jpowsour

Structural and dynamic behavior of lithium iron polysulfide Li_8FeS_5 during charge–discharge cycling

Keiji Shimoda[a,*], Miwa Murakami[a], Tomonari Takeuchi[b], Toshiyuki Matsunaga[a], Yoshio Ukyo[a], Hikari Sakaebe[b], Hironori Kobayashi[b], Eiichiro Matsubara[c]

[a] Office of Society-Academia Collaboration for Innovation, Kyoto University, Uji, Kyoto, 611-0011, Japan
[b] National Institute of Advanced Industrial Science and Technology, Ikeda, Osaka, 563-8577, Japan
[c] Department of Materials Science and Engineering, Kyoto University, Kyoto, 606-8501, Japan

HIGHLIGHTS

- Structural and dynamic behavior of Li_8FeS_5 during electrochemical cycle is studied.
- Delithiation-induced amorphization results from formation of S-S polysulfide bonds.
- Different processes are suggested for Li extraction and insertion.
- Activation energy for Li ion diffusion in Li_8FeS_5 is estimated to be 0.35 eV.

ARTICLE INFO

Keywords:
Lithium-sulfur batteries
Lithium metal polysulfide
Delithiation-induced amorphization
S-S polysulfide bond
Li diffusive motion

ABSTRACT

Lithium sulfide (Li_2S) is one of the promising positive electrode materials for next-generation rechargeable lithium batteries. To improve the electrochemical performance of electronically resistive Li_2S, a Fe-doped Li_2S-based positive electrode material (Li_8FeS_5) has been recently designed and found to exhibit excellent discharge capacity close to 800 mAh g^{-1}. In the present study, we investigate the structural and dynamic behavior of Li_8FeS_5 during charge–discharge cycling. In Li_8FeS_5, Fe ions are incorporated into the Li_2S framework structure. The Li_2S-based structure is found to transform to an amorphous phase during the charge process. The delithiation-induced amorphization is associated with the formation of S-S polysulfide bonds, indicating charge compensation by S ions. The crystalline to non-crystalline structural transformation is reversible, but Li ions are extracted from the material via a two-phase reaction, although they are inserted via a single-phase process. These results indicate that the delithiation/lithiation mechanism is neither a topotactic extraction/insertion nor a conversion-type reaction. Moreover, the activation energies for Li ion diffusion in the pristine, delithiated, and lithiated materials are estimated to be in the 0.30–0.37 eV range, which corresponds to the energy barriers for local hopping of Li ions along the Li sublattice in the Li_2S framework.

1. Introduction

Lithium sulfide (Li_2S) is one of the most promising positive electrode materials for next-generation rechargeable lithium batteries, because of its high theoretical capacity of 1167 mAh g^{-1} (1672 mAh g^{-1} in the conventional S-based notation). Its corresponding electrochemical reaction can be expressed as $Li_2S = S + 2Li^+ + 2e^-$, and involves the S^{2-}/S^0 redox couple at the average potential of 2.15 V vs. Li/Li^+ [1]. However, two well-known problems remain to be solved. The first is that both Li_2S and elemental sulfur S are electronically resistive, which gives rise to relatively poor electrochemical performance in practical applications. The other problem is the dissolution of lithium polysulfide intermediates Li_2S_x ($2 < x < 8$) into a nonaqueous electrolyte solution during the discharge, which causes an internal "shuttle" phenomenon, leading to capacity fading [2,3]. Several attempts to overcome these drawbacks have been reported. Composite electrodes with carbonaceous materials have been designed and developed to enhance the electronic conductivities of Li_2S and S. Nazar's group reported the excellent electrochemical properties of a well-designed sulfur-carbon composite electrode, where sulfur is confined within the pore structure of mesoporous carbon tubes, interconnected by carbon nanofibers to form channels [1]. A Li_2S-C composite electrode prepared

* Corresponding author.
E-mail address: k-shimoda@saci.kyoto-u.ac.jp (K. Shimoda).

https://doi.org/10.1016/j.jpowsour.2018.07.055
Received 22 May 2018; Received in revised form 9 July 2018; Accepted 12 July 2018
0378-7753/

by spark plasma sintering (SPS) showed excellent initial charge–discharge capacity and cycling stability, along with high coulombic efficiency, in an all-solid-state cell, wherein the use of inorganic solid electrolytes is expected to suppress polysulfide dissolution [4]. A ball-milled Li_2S-Fe composite was first investigated as a positive electrode material by Obrovac and Dahn [5]. Li_2S-Co and Li_2S-Cu composites were also examined [6,7]. Transition-metal (TM) ions such as Fe, Co, and Cu are considered to be effective as conducting agents and/or Li_2S decomposition catalysts. Recently, our group has developed new electrode materials from metal sulfides (TiS_2, FeS_2, and NbS_2), Li_2S and/or S, and demonstrated their good initial charge–discharge capacities and cycle stabilities [8–14]. Sakuda et al. reported the stable initial charge–discharge characteristics of amorphous TiS_4 in a nonaqueous electrolyte solution, which indicated that polysulfide dissolution was suppressed by the formation of metal-sulfur bonds [9]. They further unveiled its unique charge–discharge mechanism, involving structural changes such as the destruction/formation of S-S disulfide bonds and decrease/increase in the coordination number of Ti atoms [14]. Similarly, a Fe-doped Li_2S-based material (Li_8FeS_5) was successfully prepared and exhibited an excellent discharge capacity of ~730 mAh g^{-1} after a stepwise pre-cycling treatment [12]. The structural changes occurring in Li_8FeS_5, which became X-ray amorphous during the charge–discharge cycles, were investigated using X-ray total scattering (XTS) and X-ray absorption spectroscopy (XAS) techniques that provided structural and electronic information about the Fe/S-based framework [12,15]. These studies provided evidence for charge compensation by S ions and formation of strong S-S bonds (as in elemental sulfur) during the lithium deintercalation. However, detailed structural information about the Li environments is still lacking; this information would be important for a full understanding of the delithiation/lithiation mechanism in Li-M-S batteries (where M denotes TM ion). In the present study, we examine the changes in the local structure and dynamics of Li ions in Li_8FeS_5 during the initial charge–discharge cycle using solid-state nuclear magnetic resonance (NMR) spectroscopy as well as ^{57}Fe Mössbauer and X-ray photoelectron spectroscopy (XPS) measurements.

2. Experimental

The Fe-doped Li_2S-based material, Li_8FeS_5, was prepared as follows [12,15]: first, iron sulfide (FeS) was prepared from sponge-shaped porous Fe and S powders by the SPS method [16]. The obtained FeS powder was blended thoroughly with Li_2S powder in a molar ratio of 1:4, and the mixture was sintered by the SPS process at 600 °C for 3 min under Ar atmosphere. Finally, the sintered sample was mechanically milled for 8 h at 1000 rpm with acetylene black (AB) in a weight ratio of 9:1, to yield the Li_8FeS_5-carbon composite active material. The working electrode consisted of a mixture of the composite active material (including AB), additional AB powder, and styrene-butadiene rubber (SBR)-based binder in 71.6:25.2:0.03 wt ratio; the mixture was spread onto an Al foil with heptane and then dried under vacuum overnight. The electrode sheet was pressed into a typical thickness of ~45 μm at 10 MPa. A foil of metallic lithium (0.2 mm in thickness, > 99.9%, Honjo Metal) was used as the negative electrode, and a microporous polyolefin sheet was chosen as the separator. A solution of 1 M $LiPF_6$ dissolved in a 1:1 vol ratio mixture of ethylene carbonate (EC) and dimethyl carbonate (DMC) was used as the electrolyte solution (Tomiyama Pure Chemical Industries Ltd., battery grade). Coin-type or laminate-type cells were assembled in an Ar-filled glove box. The electrochemical measurements were performed at 30 °C. The cells were galvanostatically cycled between 2.6 and 1.0 V vs. Li/Li^+ at a current density of 46.7 mA g^{-1}. Then, they were carefully disassembled at selected charge/discharge states in a glove box and rinsed with DMC to remove the residual electrolyte solution.

X-ray diffraction (XRD) measurements were carried out by the Debye-Scherrer method using a SmartLab X-ray diffractometer (Rigaku) equipped with a multilayer mirror optics for the Mo K_α source and a D/tex Ultra one-dimensional silicon strip detector. The samples were scratched off the electrode sheets and sealed in 0.5 mmϕ borosilicate glass capillaries in a glove box.

NMR spectra were acquired on a DD2 600 spectrometer (Agilent Technologies) at a magnetic field of 14.1 T. *Operando* ^{7}Li NMR measurements were performed with a homemade wide-bore static probe, where a flat laminate-type cell was placed horizontally in the center of a 10 mm-diameter solenoid coil. A Hahn echo pulse sequence was used, with a first pulse width of 4.0 μs and an echo decay of 8 μs. Each spectrum was averaged over 30 min. ^{7}Li magic-angle spinning (MAS) NMR spectra were acquired with a wide-bore T3 MAS probe (Agilent Technologies). The powder samples were packed into 1.2 mmϕ MAS ZrO_2 rotors with airtight caps in a glove box, and spun at a spinning rate of 60 kHz during the measurements. A rotor-synchronized Hahn echo pulse sequence (π/2-τ-π-τ-acq.) was used, with a π/2 pulse width of 1.0 μs and relaxation delay of 50 s. Spin-lattice relaxation times (T_1) were acquired with the saturation-recovery technique in the temperature range from −40 to 80 °C. All spectra were referenced to a 1 M LiCl solution at 0.0 ppm.

^{57}Fe Mössbauer spectra were acquired at room temperature in constant acceleration mode with a ^{57}Co (Rh) source and a proportional counter mounted on a WissEl MB-500 Mössbauer bench. α-Fe was used for velocity calibration. The powder samples were pressed and sealed under Ar atmosphere. The spectra were deconvoluted assuming doublet components with two equivalent Lorentzian-shaped lines, from which the Mössbauer hyperfine parameters (isomer shift, IS and quadrupole splitting, QS) were extracted.

XPS measurements were performed on a PHI5000 VersaProbe II (ULVAC-PHI) photoelectron spectrometer with monochromated Al K_α radiation (1486.6 eV). The electrode sheet samples were transferred to an ultra-high vacuum sample chamber ($< 4 \times 10^{-7}$ Pa) without exposing them to air. The pass energy was set to 23.5 eV. Dual-beam charge neutralization (simultaneous irradiation with low-energy electron and Ar^+ ion beams) was applied to avoid sample charging. The spectra were acquired before and after Ar^+ ion sputtering (4 kV for 5 min). The binding energies were calibrated with respect to the C 1s signal from acetylene black at 284.6 eV. The S 2p photoelectron spectra were analyzed after Shirley-type background subtraction.

3. Results and discussion

3.1. Sample characterization and charge–discharge profile

Fig. 1 shows the scanning electron microscope (SEM) image of the Li_8FeS_5 electrode, along with energy-dispersive X-ray spectrometry (EDS) images at S and Fe K-edges. The EDS images indicate that S and Fe atoms are uniformly dispersed in the active material. The chemical composition of the sample was determined to be $Li_{7.8}Fe_{1.0}S_{4.8}$ by inductively coupled plasma-atomic emission spectrometry (ICP-AES) analysis [12]. The electrical conductivity of Li_8FeS_5 was in the range 10^{-2} to 10^{-3} S cm^{-1}, which was much higher than that of Li_2S ($< 10^{-10}$ S cm^{-1}) [12]. Therefore, the Fe doping in Li_2S increased the electrical conductivity, as expected.

Fig. 2 shows the charge–discharge profile of the Li//Li_8FeS_5 cell for the initial cycle. Different sampling points are plotted in the figure. The charge capacity at 2.6 V was approx. 600 mAh g^{-1}, which is smaller than the theoretical capacity of 789 mAh g^{-1}, revealing the $Li_{\sim 2}FeS_5$ composition of the material. Two voltage plateau (or sloping) regions were observed during the discharge process. The discharge capacity delivered during the upper voltage plateau reached 600 mAh g^{-1}, corresponding to the full reinsertion of Li ions in the material at 1.6 V. Additional capacity was delivered at the second voltage plateau of ~1.4 V, and the capacity reached approx. 780 mAh g^{-1} at 1.0 V. The material composition was close to $Li_{\sim 10}FeS_5$.

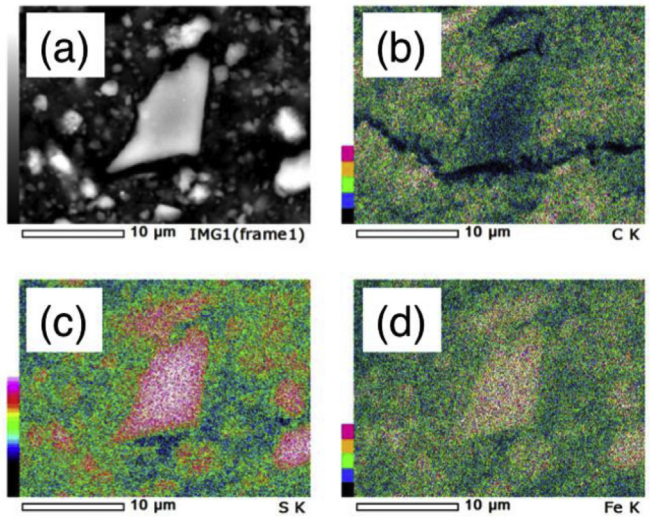

Fig. 1. SEM-EDS images of the pristine Li_8FeS_5 electrode. Backscattered electron image (a) and EDS maps for (b) C, (c) S, and (d) Fe.

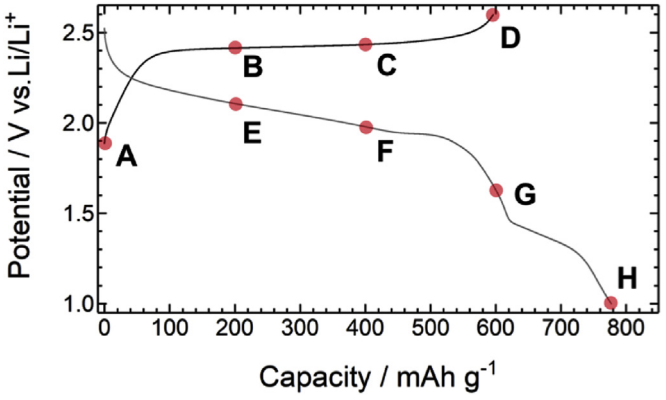

Fig. 2. Charge–discharge profile of the Li//Li_8FeS_5 cell for the initial cycle. The sampling points marked on the figure correspond to the pristine electrode (A) and to electrodes charged to 200 mAh g^{-1} (B), 400 mAh g^{-1} (C), 2.6 V (D), and subsequently discharged to 200 mAh g^{-1} (E), 400 mAh g^{-1} (F), 600 mAh g^{-1} (G), and 1.0 V (H).

3.2. Structural changes during charge–discharge cycling

Fig. 3 shows the XRD profiles of representative samples

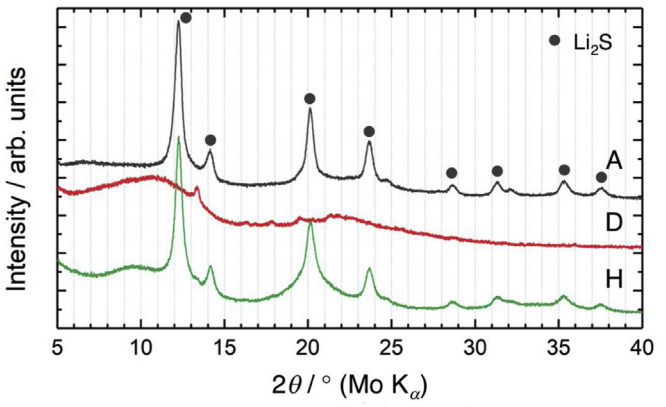

Fig. 3. XRD profiles for the pristine electrode (A) and the electrodes charged to 2.6 V (D) and discharged to 1.0 V (H). Almost identical sample volumes were irradiated by X-rays in all cases.

disassembled at the points indicated in Fig. 2. The diffraction profile of the pristine electrode (A) could be indexed to the *Fm*–3m space group, indicating that Li_8FeS_5 has a Li_2S-based framework structure, as mentioned in previous studies [12,15]. The diffraction peaks almost vanished in the sample disassembled at 2.6 V (D), suggesting the occurrence of delithiation-induced amorphization. The Li_2S-based structure was recovered after discharging to 1.0 V (H). This crystalline to non-crystalline structural transformation seems to occur reversibly during the charge–discharge cycles. Synchrotron-radiation X-ray pair distribution function (PDF) analyses of the charged and discharged materials are currently in progress.

To understand the delithiation/lithiation mechanism from the viewpoint of Li local structure, *operando* ^{7}Li NMR measurements were carried out on the Li//Li_8FeS_5 cell, with pulse conditions optimized for the Li_8FeS_5 signal (Fig. 4). Three signals were observed in the lowermost spectrum of Fig. 4a, before the electrochemical tests. The sharp peaks at 0 and 250 ppm originate from the $LiPF_6$ salt in the electrolyte solution and the Li metal used as the counter electrode, respectively. Li_8FeS_5 gives rise to a broad signal centered at −200 ppm, which is influenced by the strong dipolar interaction between the ^{7}Li nucleus and the unpaired electron on the Fe ion [17–19]. In addition, the peak position of the Li_8FeS_5 signal differs from the isotropic shift, due to the bulk magnetic susceptibility (BMS) effect [17–19]. During the delithiation process, the Li_8FeS_5 signal decreased in intensity, while the peak position shifted to higher frequencies (Fig. S1a). On the other hand, the lithiation process down to 1.5 V proceeded differently, with an increase in signal width (Fig. S1b). This strongly suggests different mechanisms for the delithiation and lithiation processes. Then, the signal decreased again upon further discharging down to 1.0 V. Fig. 4b shows the evolution of the integrated intensity of the Li_8FeS_5 signal. The intensity decreased linearly during the charge process, and the Li contents estimated from the NMR spectra were almost identical to those obtained from the charge capacities. During the discharge process, the intensity first increased upon discharging down to 1.5 V, and then decreased below 1.5 V. The Li contents were smaller than those estimated from the discharge capacities. The intensity loss below 1.5 V partly derives from the incomplete excitation of the broader signal component. We confirmed that the Li content in the electrode disassembled at 1.0 V was almost identical to that estimated from the capacity by the ICP-AES measurements. These results can be interpreted as indicating a strong contribution from paramagnetic spins on the discharge process. The *operando* spectra in the second cycle showed an apparent increase in signal intensity, until the charging voltage reached 2.3 V. After that, the evolution of the spectra was similar to that observed in the initial cycle, although the overall signal intensities were reduced. Therefore, we investigated the detailed structural changes in the Li environments during the initial cycle.

Fig. 5 shows high-resolution ^{7}Li MAS NMR spectra for the electrode samples disassembled at the points shown in Fig. 2. The spectra were normalized by the scan number and sample weight in the rotors. All samples showed a sharp peak at 0 ppm with several spinning sidebands (SSBs), indicating the diamagnetic nature of the observed ^{7}Li signal. It is expected that Fe^{2+} and S^{2-} ions balance the charge in Li_8FeS_5. A structural model was recently proposed for Li_8FeS_5, in which a Fe^{2+} ion and a vacancy replace two tetrahedral Li sites in the Li_2S structure [12,15]. The tetrahedrally coordinated Fe^{2+} ($3d^6$ electronic configuration) should be paramagnetic, whereas the Fe^{2+} ions are diamagnetic only in the low-spin state of octahedral environments such as FeS_2 pyrite and marcasite structures. Therefore, a significant ^{7}Li peak shift should be observed for Li_8FeS_5 due to the Fermi contact interaction between the Li ions and the paramagnetic spins [20]. However, we could not detect other signals between −10,000 and 10,000 ppm. The Li contents were estimated from the ^{7}Li signals, based on the linear relationship between integrated NMR intensity and Li content in the sample rotor for the diamagnetic salts (Li_2CO_3 and LiF). We found that the ^{7}Li signal intensity observed in the pristine electrode corresponded

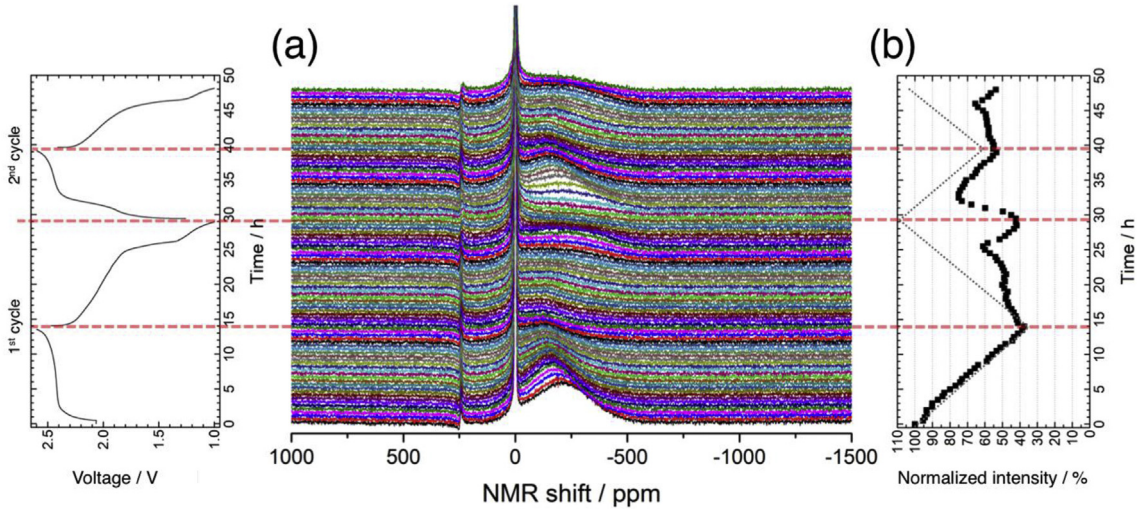

Fig. 4. (a) Time evolution of *operando* ^{7}Li NMR spectra of the Li//Li_8FeS_5 cell, along with corresponding charge–discharge profile. (b) Normalized intensity plot of the Li_8FeS_5 signal. The dotted grey lines are a guide to the eye.

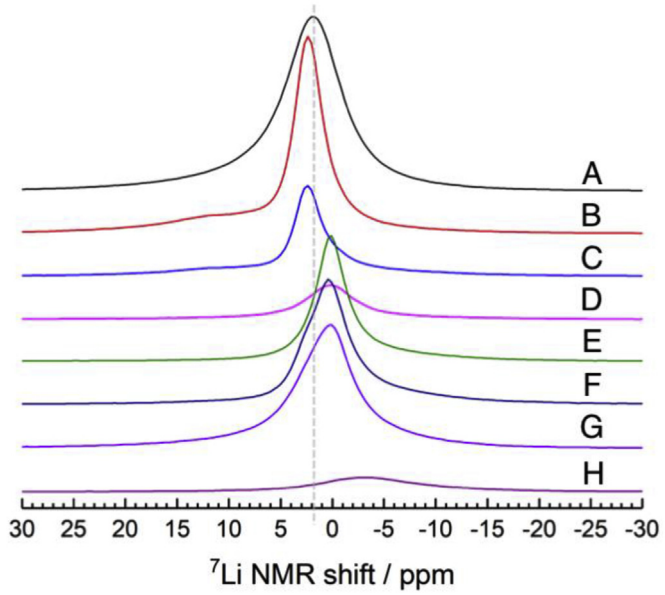

Fig. 5. ^{7}Li MAS NMR spectra of electrode samples disassembled at the points marked in Fig. 2.

to 34% of the Li ions in the active material, Li_8FeS_5. The remaining 66% of Li ions would be undetectable, due to the strong through-bond interaction with the paramagnetic spins [20,21]. Therefore, we believe that the observed diamagnetic ^{7}Li signal can be attributed to Li ions slightly away from the paramagnetic Fe ions within the Li_8FeS_5 structure, but not from diamagnetic impurities such as unreacted Li_2S.

The detailed examination of the spectra provided some insight into the delithiation/lithiation mechanism. The pristine sample (A) showed an isotropic signal at 1.9 ppm, with a full width at half maximum (FWHM) of 1.5 kHz. In the case of the samples disassembled at charging capacities of 200 and 400 mAh g^{-1} (B and C, respectively), the peak position slightly shifted to 2.4 ppm with an additional signal at ~10 ppm, and the peak width became narrower (0.8 kHz) compared with that of the pristine sample. Then, the peak position shifted back to 0.2 ppm, with a width of 1.3 kHz at 2.6 V (D). These results indicate that the Li deintercalation proceeds first as a single-phase reaction (A→B), then as a two-phase reaction during the potential plateau (B→C), and finally as a single-phase process (C→D). The spectra of the samples disassembled at discharging capacities of 200, 400, and 600 mAh g^{-1} (E, F, and G, respectively) showed an identical isotropic shift of 0.2 ppm; however, the peak widths increased from 0.8 to 1.4 kHz without increase in peak height. Then, an intensity decrease was observed for the sample discharged at 1.0 V (H), with an isotropic shift at −3.2 ppm and a width of 2.5 kHz. Furthermore, this sample presented significant SSBs (Fig. S2a), indicating a strong dipolar interaction with the paramagnetic spins. These results indicate that Li intercalation proceeds as a single-phase reaction (D→E→F→G); this process is different from the delithiation. Different Li environments were present in samples disassembled at charge/discharge states with similar Li contents (A-G, B-F, and C-E). Considering the above XRD results, we believe that the crystalline structure of Li_8FeS_5 transforms to an amorphous state mainly via a two-phase reaction during the delithiation, whereas the amorphous structure reverts to the crystalline structure via a single-phase reaction during the lithiation. Further lithiation produced the second potential plateau between 1.5 and 1.0 V, indicating that another lithiation mechanism should be considered. The strongly modified spectral feature suggests charge compensation by paramagnetic Fe ions (G→H). The intercalated Li ions became spatially closer to the Fe ions, showing a much stronger dipolar interaction-induced signal broadening. The intensity evolution for the disassembled samples (Fig. S2b) was similar to that observed for the *operando* measurements (Fig. 4b): the observed NMR intensities for the discharged samples were smaller than those expected from the capacities. The undetected Li ions would experience a strong Fermi-contact interaction and/or dipolar interaction with the paramagnetic spins, causing the ultrafast ^{7}Li signal relaxation to be undetectable [19–21]. These results suggest that Li intercalation involves structural and electronic changes affecting the Fe ions, which in turn induce ^{7}Li line broadening and intensity loss during the discharge process.

To investigate the changes taking place in the Fe environment, ^{57}Fe Mössbauer spectra were obtained for representative samples (Fig. 6). The Mössbauer hyperfine parameters (IS and QS) extracted from the spectra are listed in Table 1. The IS parameter is related to the valence state of Fe ions: it decreases with increasing s-electron density at the Fe nucleus, as a consequence of the reduced shielding of the 3s and 4s electrons upon removal of the d electron when changing from the $3d^6$ (Fe^{2+}) to the $3d^5$ (Fe^{3+}) configuration [22]. The present samples exhibited IS values different from those of FeS (0.78 mm s^{-1}), Li_2FeS_2 (0.48, 0.50 mm s^{-1}), and superparamagnetic Fe (−0.13 mm s^{-1}) [23–25]. The IS value obtained for the pristine material (A) was within the range of values expected for high-spin Fe^{3+} ions tetrahedrally coordinated by S, based on the empirical relationship IS_{tet} = 1.68–0.5 m + (where m+ is the mean valence) introduced by Goodenough [26],

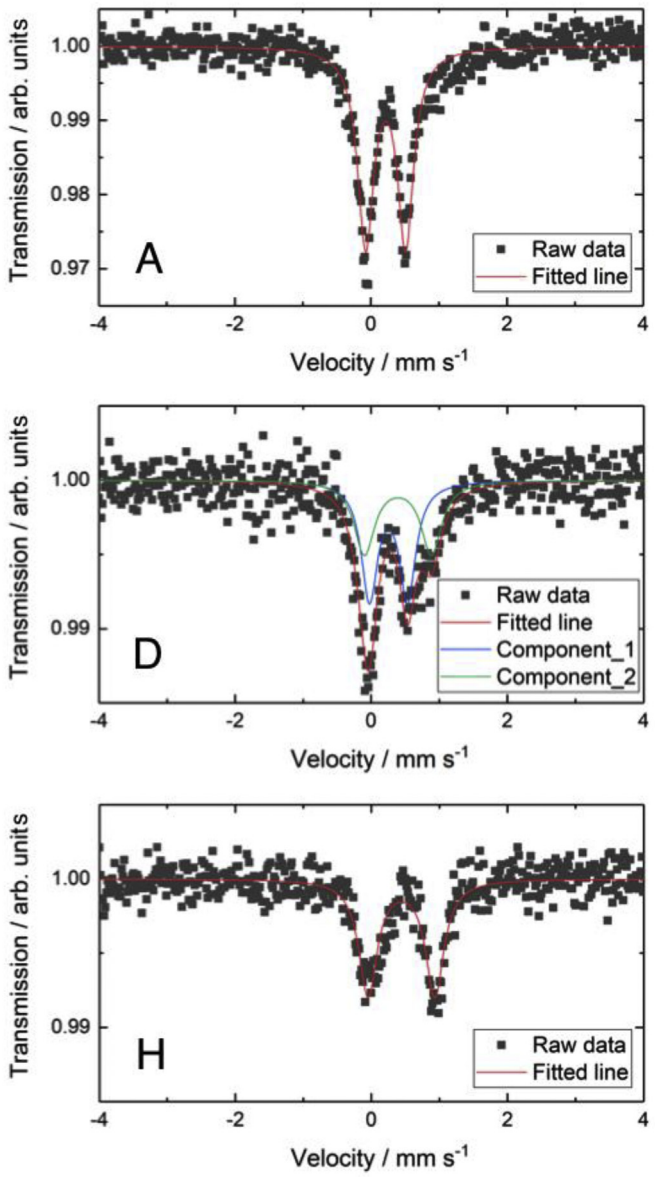

Fig. 6. ^{57}Fe Mössbauer spectra for the pristine electrode (A) and the electrodes charged to 2.6 V (D) and discharged to 1.0 V (H).

Table 1
^{57}Fe Mössbauer parameters, isomer shift (IS) and quadrupole splitting (QS), for the pristine electrode (A) and the electrodes charged to 2.6 V (D) and discharged to 1.0 V (H).

Sample		IS/mm s^{-1}	QS/mm s^{-1}	FWHM/mm s^{-1}	Area ratio/%
A	–	+0.22	0.59	0.29	100
D	#1	+0.26	0.56	0.29	56
	#2	+0.39	0.98	0.36	44
H	–	+0.44	0.98	0.33	100

and was also smaller than the IS values of FeS_2 pyrite (0.31 mm s^{-1}) and marcasite (0.27 mm s^{-1}), which have octahedrally coordinated low-spin Fe^{2+} ions [27]. Therefore, the Fe ions in Li_8FeS_5 are apparently trivalent, although this seems inconsistent with the expected formal valence of iron (i.e., Fe^{2+}) in Li_8FeS_5. The Mössbauer spectrum of the sample disassembled at 2.6 V (D) could be fitted with two doublet components in an almost equimolar ratio, indicating the presence of two distinct Fe environments in $Li_{\sim 2}FeS_5$: one with IS and QS values similar to those of the pristine material, and the other with larger values (Table 1). The Mössbauer spectrum of the sample disassembled at 1.0 V (H) was fitted by a single component. The IS and QS values were close to those of the second component of the spectrum of the sample disassembled at 2.6 V. The increase in IS suggests a decrease in the Fe valence [22,26]. Moreover, the increase in QS denotes a higher symmetry distortion around the Fe ion. Therefore, these results may indicate that the Fe ions are gradually reduced from Fe^{3+} to $Fe^{2.5+}$ during the charge–discharge process. Alternatively, the results may also reflect a change from tetrahedral to octahedral coordination of the high-spin Fe^{3+} ions, because an IS value of 0.35 mm s^{-1} can be predicted for the octahedral Fe^{3+} ion via the empirical relationship IS_{oct} = 1.85–0.5 m+ [26]. It is interesting to note that a change in the Ti coordination number during the charge–discharge process was suggested for amorphous TiS_4 [14]. Therefore, the Mössbauer results can be interpreted as follows: the coordination increase of Fe^{3+} ions from the tetrahedral to the octahedral environment occurs along with the structural amorphization during the charge process. Then, the Li_2S framework is recovered during the discharge, suggesting that the tetrahedral Fe coordination is also recovered, but its valence state is reduced to 2.5+.

Fig. 7 shows the S 2p and Fe 2p XPS spectra for the pristine electrode and some of the charged and discharged samples (A, D, G, and H). We confirmed that the Ar^+ ion sputtering hardly affected the spectral shape and peak positions, but enhanced the spectral intensity by peeling off the adsorbed surface layer. The S 2p spectrum of the pristine electrode (A) can be described by three sets of doublet peaks ($p_{3/2}$ and $p_{1/2}$, due to the spin-orbit splitting), each with an energy separation of 1.2 eV and an intensity ratio of 2:1. The spectral deconvolution is shown in Fig. S3. The three $p_{3/2}$ peaks at 161.2, 162.2, and 163.5 eV were attributed to S^{2-}, S^- (S_2^{2-}), and S^0 states, respectively (for reference, the corresponding peaks of $KFeS_2$, FeS_2, and S_8 are located at 161.4, 162.5, and 163.7 eV, respectively) [28–31]. It is worth noting that the S^{2-} signal of Li_8FeS_5 is located at a slightly higher binding energy than that of Li_2S (160.0 eV, as measured in this work and in Ref. [32]), suggesting a more covalent character of bonds involving sulfur in the former ((Li, Fe)-S vs. Li-S). We estimated a S^{2-}:S^-:S^0 intensity ratio of 61:16:23, although only the S^{2-} species was expected to be present, based on the chemical composition. The escape depth of S 2p photoelectrons is approximately 15 monolayers from the particle surface when the Al K_α source is used. Therefore, ~90% of the S 2p total intensity represents signals from the subsurface-to-bulk region (< 50 Å), and the remaining ~10% originates from the outermost surface layers that may experience surface reconstruction [33]. We confirmed that the S^{2-}:S^-:S^0 intensity ratio was 90:7:3 in Li_2S. Therefore, Li_8FeS_5 exhibits a variety of sulfur bonding environments, ranging from mostly ionic to covalent. The excess S^- species in the pristine material would most likely correspond to the S ions near the Li vacancy in the Li_8FeS_5 structure [15]. The S 2p spectrum for the sample charged to 2.6 V (D) showed a significant increase in the signal corresponding to the S^0 component (S^{2-} (161.5 eV):S^- (161.9 eV):S^0 (163.7 eV) = 7:22:71), suggesting that the Li extraction was charge-compensated by S through the formation of S-S polysulfide bonds [34]. This is consistent with the changes in the X-ray absorption near-edge structure (XANES) spectra at the S K-edge reported in a previous study [12]. This result indicates that Fe doping in the Li_2S structure confines the soluble polysulfide species within the solid, probably due to the presence of strong Fe-S covalent bonds [9], suppressing the internal polysulfide shuttle phenomenon observed in conventional Li–S batteries [2,3]. In addition, the formation of S-S polysulfide bonds leads to structural amorphization of the material [12]. At the discharging capacity of 600 mAh g^{-1} (G), where the Li content in the material is expected to be nearly equal to that in the pristine sample, the fraction of the S^0 component decreased (S^{2-} (160.8 eV):S^- (162.0 eV):S^0 (163.6 eV) = 45:21:35). After discharging to 1.0 V (H), the S environment almost returned to that of the pristine material (S^{2-} (160.5 eV):S^- (162.0 eV):S^0 (163.7 eV) = 65:20:15, see

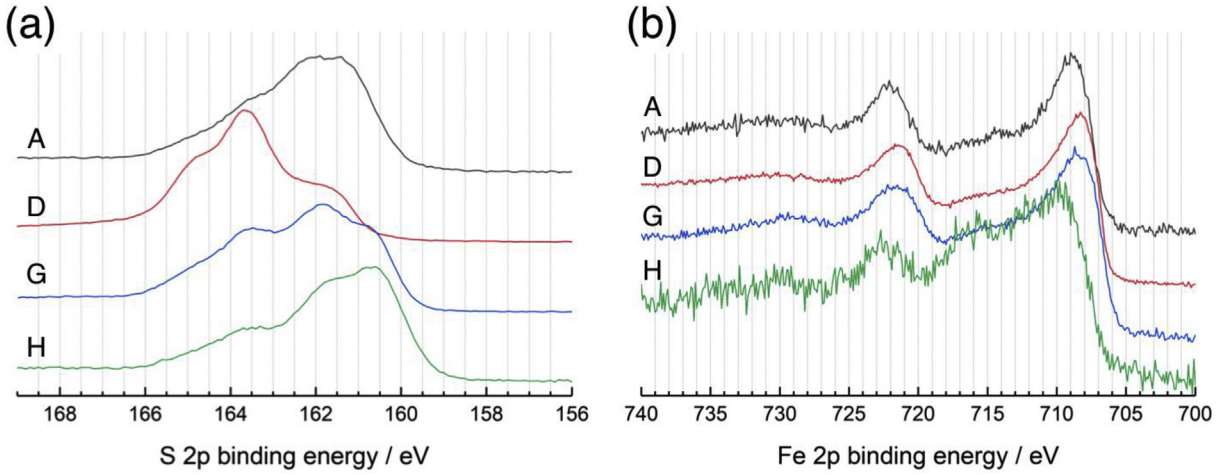

Fig. 7. (a) S 2p and (b) Fe 2p core-level XPS spectra after Ar^+ ion sputtering measured for the pristine electrode (A) and for the electrodes charged to 2.6 V (D) and discharged to 600 mAh g^{-1} (G) and 1.0 V (H). For clarity, the spectral intensities are normalized to unity.

also Fig. S4). The chemical shift of the S^{2-} component was slightly shifted to lower binding energies compared to that in the pristine material, suggesting that the sulfur bonding environments are more ionic and close to Li_2S due to excessive lithiation. The Fe 2p core-level spectra are shown in Fig. 7b. The spectra are split into two components, $p_{3/2}$ (705–718 eV) and $p_{1/2}$ (718–735 eV), due to the spin-orbit coupling. The binding energy of the Fe $2p_{3/2}$ peak in the pristine material (~708.9 eV) was higher than that of FeS_2 (706.6, 707.0 eV) and lower than that of FeS (710.1, 711.9 eV), but also close to the corresponding values for $KFeS_2$ (708.5 eV) and $CuFeS_2$ (707.8 eV) [28,29,35,36]. The latter two compounds contain Fe^{3+} ions in a tetrahedral environment. This indicates that the Fe ions in the pristine material are trivalent, in agreement with the Mössbauer parameter discussed above, although this evidence is not conclusive, due to the lack of reliable chemical shift references. The Fe $2p_{3/2}$ peak shifted slightly to a lower binding energy of 708.3 eV at 2.6 V, but was located at a higher energy (~709.5 eV) at 1.0 V. This behavior seems to be inversely correlated with that of the charge compensation by S, with the Fe valence decreasing during the charge and increasing during the discharge. This is apparently inconsistent with the Mössbauer results discussed above, and a reasonable explanation for this discrepancy is difficult. Therefore, we simply conclude that some changes in the valence and/or coordination state of the Fe ions occur during the charge–discharge cycling.

3.3. Activation energies for local flip motions of Li ions during charge–discharge cycling

Variable-temperature ^{7}Li NMR relaxometry is a powerful tool to study the dynamical properties of Li ions in solid electrolyte and electrode materials [37–43]. NMR signal relaxation is considered to be effectively induced by atomic motion, because the transitions between the energy levels of a spin system are influenced by the fluctuations of internal magnetic and electric fields. In particular, T_1 relaxation measurements are sensitive to atomic displacements with jump rates on the order of the applied Larmor frequency, corresponding to migration on a short-range scale. Here, we utilized the ^{7}Li spin-lattice relaxation rates in the laboratory frame R_1 (= $1/T_1$) to examine the Li ion dynamics in pristine Li_8FeS_5 and its delithiated and lithiated counterparts. Fig. 8a shows the temperature dependence of ^{7}Li R_1 values for the pristine electrode, as a reference. The observed linear dependence of $\log_{10} R_1$ on $1/T$ indicates that the motion responsible for the ^{7}Li relaxation takes place in the region of the strong collision limit in the temperature range studied, for which the correlation time of motion, τ_c, satisfies $\omega_0\tau_c \gg 1$ (where ω_0 is the Larmor frequency for ^{7}Li) [39,44]. In the strong collision limit, the rate R_1 due to the ^{7}Li-^{7}Li homonuclear dipolar

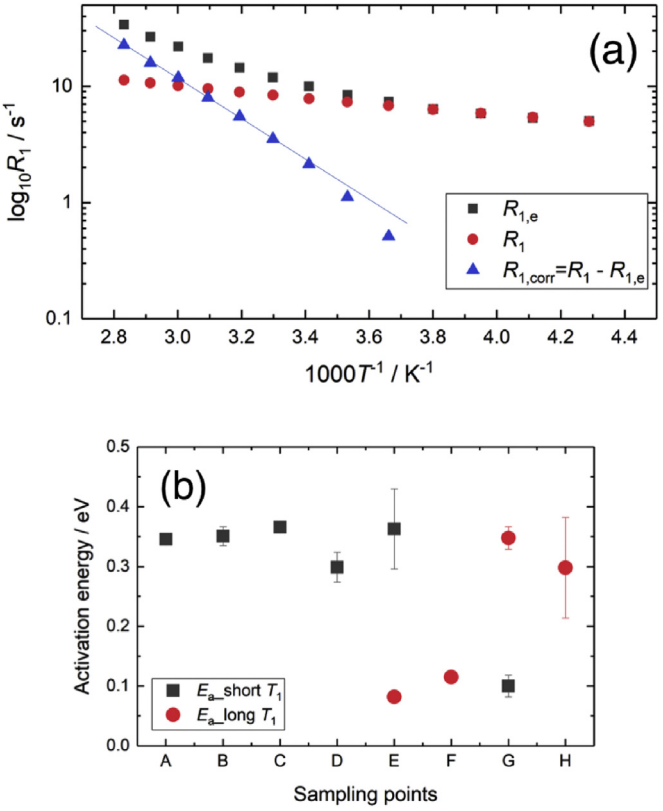

Fig. 8. (a) Temperature dependence of ^{7}Li NMR spin-lattice relaxation rate R_1 for the pristine electrode. The activation energy E_a for the local flip motions was determined from the background-corrected rate $R_{1,corr}$, whose least-squares fit was performed between 20 and 80 °C. (b) Activation energies determined for the delithiated and lithiated samples. The error bars denote standard errors of least-squares fits. The E_a value for the short T_1 component of sample F is not shown because its $\log_{10} R_1$ vs. $1/T$ plot did not show a linear relationship.

interaction becomes proportional to $1/(\omega_0{}^2\tau_c)$. Assuming a single correlation time for the motion with an Arrhenius dependence on the temperature ($\tau_c{}^{-1} = \tau_0{}^{-1}\exp(-E_a/k_BT)$, where k_B is the Boltzmann constant), the activation energy E_a can be determined by a least-squares fitting of the plots to a straight line. At the low temperatures studied here (≤–10 °C), the slope of the Arrhenius plot became shallow, due to background relaxation mechanisms arising from paramagnetic impurities, lattice vibrations, and/or the interaction of the ^{7}Li spins with

conduction electrons [38,40–42]. We subtracted the background contribution, $R_{1,e}$, by extrapolating a power-law fit, $R_{1,e} = s'T^{\kappa}$, and the obtained $\kappa \approx 2$ was consistent with the interaction of the ^{7}Li spins with phonons [38,40,42]. The activation energy for the pristine material was estimated to be 0.35 eV after the background correction. The Li diffusion pathways in the Li_2S structure were examined by the nudged elastic band (NEB) method, coupled with density functional theory (DFT) calculations [45]. The Li diffusion along the Li sublattice (with shortest Li-Li distance of ~2.9 Å) was the most favorable, and the calculated diffusion barrier was 0.27 eV. This value is expected to increase in the Fe-doped Li_2S structure, because of its smaller lattice parameter [15]: our preliminary transition state calculation for the Fe-doped Li_2S supercell structure yielded an energy barrier of 0.31 eV. Therefore, the activation energy obtained in the present study corresponds to the energy barrier for a Li ion jumping to an adjacent vacancy site. This motion corresponds to the local diffusion of Li ions along the Li sublattice in the Li_2S-based structure. In the strong collision limit, the T_1 relaxation is associated with the local flip motions of Li ions along a few sites, instead of the long-range diffusion with successive flip motions. The diffusion of Li ions on a longer-range scale can be probed when T_1 data in the region corresponding to the weak collision limit are available [39,44]. This would necessitate T_1 measurements at higher temperatures; however, these measurements could not be performed because the sulfide samples were easily degraded upon heating. It should be noted that the activation energy for long-range Li diffusion in Li_8FeS_5 would be larger than 0.35 eV, the barrier corresponding to the local flip motions. This is because the introduction of Fe ions in the Li_2S framework results in a highly disordered Li_8FeS_5 structure, as evidenced by XRD [12,15]. In a previous study, the Li diffusion parameters of a lithium metal polysulfide, hexagonal $Li_{0.7}TiS_2$ (h-$Li_{0.7}TiS_2$), were determined using several NMR relaxometry techniques [38]. The activation energies (obtained with different techniques) for both the local jumps and long-range diffusion of Li ions in h-$Li_{0.7}TiS_2$ were almost identical (0.34–0.38 eV). These E_a values are close to that obtained in the present study, although the corresponding structures (and therefore Li diffusion pathways) are different.

The activation energies determined for the delithiated and lithiated samples are plotted in Fig. 8b. A linear dependence of $\log_{10} R_1$ on $1/T$ was observed for all samples. Two T_1 components were obtained for the lithiated samples, except for that disassembled at 1.0 V (H). Almost constant activation energies (0.30–0.37 eV) were obtained for all samples, although those of the second components of the lithiated samples were much lower (~0.1 eV). We believe that the much lower energies obtained for the latter components are fictitious, due to the larger background contribution [38,42]. This result is in contrast with those of previous studies, where decreasing E_a values upon lithium deintercalation or intercalation have been reported for $LiCoO_2$ and $Li_4Ti_5O_{12}$ [37,41]. The E_a decreases were associated with the increased concentration of Li vacancies and the widening of diffusion channels, due to the increased Coulomb repulsion between oxygen layers in the layered structure or to the Coulomb repulsion caused by the simultaneous occupation of neighboring Li sites in the spinel structure [41]. In the present case, the constant E_a values for Li motions during the delithiation process appear consistent with a two-phase reaction process between the Li-rich and Li-poor phases. Li intercalation involves the structure reversal from the Li-poor amorphous state to the Li_2S-based structure, and the E_a values for Li motions in the lithiated states are expected to be similar to each other.

4. Conclusions

The delithiation/lithiation process of Li_8FeS_5 was investigated in detail. The XRD profiles confirmed the Fe-doped Li_2S structure of Li_8FeS_5, which then reversibly transformed to an amorphous structure during the charge–discharge cycle. Based on *operando* ^{7}Li NMR and *ex situ* ^{7}Li MAS NMR measurements, it was shown that different Li environments were present in charge and discharge states with similar Li contents: Li ions were extracted from the material in a two-phase reaction, whereas they were inserted in a single-phase process. The structural and/or valence state changes of the Fe ions in the material were determined from ^{57}Fe Mössbauer spectroscopy measurements. XPS measurements confirmed that charge compensation was mainly accomplished by S, indicating the formation and breakage of S-S polysulfide bonds. The formation of S-S bonds altered the local structure during the delithiation process, leading to an amorphous structure. This delithiation-induced amorphization implies that the delithiation/lithiation mechanism is neither a topotactic insertion/extraction nor a conversion-type reaction. The E_a values for the local flip motions of Li ions in the pristine, delithiated, and lithiated materials were determined from the analysis of ^{7}Li NMR spin-lattice (T_1) relaxation times. The obtained E_a values were found to be almost constant in the range of 0.30–0.37 eV, associated with the local hopping of Li ions along the Li sublattice in the Li_2S framework. This suggests that the local structural rearrangements induced by the formation and breakage of S-S polysulfide bonds during the charge–discharge cycle hardly affect the local Li motions in Li_xFeS_5. We believe that the present work serves as a guide for the design and development of novel lithium metal polysulfide (Li-M-S) electrode materials, where TM ion doping improves electrical conductivity and suppresses polysulfide dissolution, eventually resulting in better electrochemical performance.

Acknowledgements

This work was supported by the Research and Development Initiative for Scientific Innovation of New Generation Batteries 2 (RISING2) project funded by the New Energy and Industrial Technology Development Organization, Japan. The authors thank Mr. Takashi Moroishi for his support in the sample preparation and NMR measurements. The authors are grateful to Dr. Takashi Segi of Kobelco Research Institute, Inc. and Prof. Satoru Nakashima of Hiroshima University for their support in the ^{57}Fe Mössbauer measurements.

Appendix A. Supplementary data

Supplementary data related to this article can be found at https://doi.org/10.1016/j.jpowsour.2018.07.055.

References

[1] X. Ji, L.F. Nazar, J. Mater. Chem. 20 (2010) 9821–9826.
[2] R.D. Rauh, F.S. Shuker, J.M. Marston, S.B. Brummer, J. Inorg. Nucl. Chem. 39 (1977) 1761–1766.
[3] Q. Liu, D. Mu, B. Wu, L. Wang, L. Gai, F. Wu, RSC Adv. 7 (2017) 33373–33377.
[4] T. Takeuchi, H. Kageyama, K. Nakanishi, M. Tabuchi, H. Sakaebe, T. Ohta, H. Senoh, T. Sakai, K. Tatsumi, J. Electrochem. Soc. 157 (2010) A1196–A1201.
[5] M.N. Obrovac, J.R. Dahn, Electrochem. Solid state Lett. 5 (2002) A70–A73.
[6] Y. Zhou, C. Wu, H. Zhang, X. Wu, Z. Fu, Electrochim. Acta 52 (2007) 3130–3136.
[7] A. Hayashi, R. Ohtsubo, T. Ohtomo, F. Mizuno, M. Tatsumisago, J. Power Sources 183 (2008) 422–426.
[8] T. Takeuchi, H. Kageyama, K. Nakanishi, Y. Inada, M. Katayama, T. Ohta, H. Senoh, H. Sakaebe, T. Sakai, K. Tatsumi, H. Kobayashi, J. Electrochem. Soc. 159 (2012) A75–A84.
[9] A. Sakuda, N. Taguchi, T. Takeuchi, H. Kobayashi, H. Sakaebe, K. Tatsumi, Z. Ogumi, Electrochem. Commun. 31 (2013) 71–75.
[10] A. Sakuda, N. Taguchi, T. Takeuchi, H. Kobayashi, H. Sakaebe, K. Tatsumi, Z. Ogumi, Solid State Ionics 262 (2014) 143–146.
[11] A. Sakuda, T. Takeuchi, K. Okamura, H. Kobayashi, H. Sakaebe, K. Tatsumi, Z. Ogumi, Sci. Rep. 4 (2014) 4883.
[12] T. Takeuchi, H. Kageyama, K. Nakanishi, M. Ogawa, T. Ohta, A. Sakuda, H. Sakaebe, H. Kobayashi, Z. Ogumi, J. Electrochem. Soc. 162 (2015) A1745–A1750.
[13] A. Sakuda, T. Takeuchi, M. Shikano, K. Ohara, K. Fukuda, Y. Uchimoto, Z. Ogumi, H. Kobayashi, H. Sakaebe, J. Ceram. Soc. Jpn. 125 (2017) 268–271.
[14] A. Sakuda, K. Ohara, K. Fukuda, K. Nakanishi, T. Kawaguchi, H. Arai, Y. Uchimoto, T. Ohta, E. Matsubara, Z. Ogumi, T. Okumura, H. Kobayashi, H. Kageyama, M. Shikano, H. Sakaebe, T. Takeuchi, J. Am. Chem. Soc. 139 (2017) 8796–8799.
[15] T. Takeuchi, H. Kageyama, N. Taguchi, K. Nakanishi, T. Kawaguchi, K. Ohara, K. Fukuda, A. Sakuda, T. Ohta, T. Fukunaga, H. Sakaebe, H. Kobayashi,

E. Matsubara, Solid State Ionics 320 (2018) 387–391.
[16] T. Takeuchi, H. Sakaebe, H. Kageyama, T. Sakai, K. Tatsumi, J. Electrochem. Soc. 155 (2008) A679–A684.
[17] N.M. Trease, L. Zhou, H.J. Chang, B.Y. Zhu, C.P. Grey, Solid State Nucl. Magn. Reson. 42 (2012) 62–70.
[18] L. Zhou, M. Leskes, A.J. Ilott, N.M. Trease, C.P. Grey, J. Magn. Reson. 234 (2013) 44–57.
[19] K. Shimoda, M. Murakami, H. Komatsu, H. Arai, Y. Uchimoto, Z. Ogumi, J. Phys. Chem. C 119 (2015) 13472–13480.
[20] C.P. Grey, N. Dupré, Chem. Rev. 104 (2004) 4493–4512.
[21] M. Ménétrier, I. Saadoune, S. Levasseur, C. Delmas, J. Mater. Chem. 9 (1999) 1135–1140.
[22] J.T. Hoggins, H. Steinfink, Inorg. Chem. 15 (1976) 1682–1685.
[23] C.H.W. Jones, P.E. Kovacs, R.D. Sharma, R.S. McMillan, J. Phys. Chem. 94 (1990) 832–836.
[24] C.H.W. Jones, P.E. Kovacs, R.D. Sharma, R.S. McMillan, J. Phys. Chem. 94 (1990) 4325–4329.
[25] K. Takada, Y. Kitami, T. Inada, A. Kajiyama, M. Kouguchi, S. Kondo, M. Watanabe, M. Tabuchi, J. Electrochem. Soc. 148 (2001) A1085–A1090.
[26] J.B. Goodenough, G.A. Fatseas, J. Solid State Chem. 41 (1982) 1–22.
[27] A.A. Temperley, H.W. Lefevre, J. Phys. Chem. Solid. 27 (1966) 85–92.
[28] H. Binder, Z. Naturforsch. B Chem. Sci. 28 (1973) 255–262.
[29] J.R. Mycroft, G.M. Bancroft, N.S. McIntyre, J.W. Lorimer, I.R. Hill, J. Electroanal. Chem. 292 (1990) 139–152.
[30] R.StC. Smart, W.M. Skinner, A.R. Gerson, Surf. Interface Anal. 28 (1999) 101–105.
[31] T. Matsuyama, M. Deguchi, K. Mitsuhara, T. Ohta, T. Mori, Y. Orikasa, Y. Uchimoto, Y. Kowada, A. Hayashi, M. Tatsumisago, J. Power Sources 313 (2016) 104–111.
[32] Y. Jung, B. Kang, Phys. Chem. Chem. Phys. 18 (2016) 21500–21507.
[33] M.E. Fleet, S.L. Harmer, X. Liu, H.W. Nesbitt, Surf. Sci. 584 (2005) 133–145.
[34] E.D. Grayfer, E.M. Pazhetnov, M.N. Kozlova, S.B. Artemkina, V.E. Fedorov, ChemSusChem 10 (2017) 4805–4811.
[35] J.C. Carver, G.K. Schweitzer, T.A. Carlson, J. Chem. Phys. 57 (1972) 973–982.
[36] A. Ghahremaninezhad, D.G. Dixon, E. Asselin, Electrochim. Acta 87 (2013) 97–112.
[37] K. Nakamura, H. Ohno, K. Okamura, Y. Michihiro, T. Moriga, I. Nakabayashi, T. Kanashiro, Solid State Ionics 177 (2006) 821–826.
[38] M. Wilkening, P. Heitjans, Phys. Rev. B 77 (2008) 024311.
[39] M. Wilkening, P. Heitjans, ChemPhysChem 13 (2012) 53–65.
[40] J. Langer, V. Epp, P. Heitjans, F.A. Mautner, M. Wilkening, Phys. Rev. B 88 (2013) 094304.
[41] W. Schmidt, P. Bottke, M. Sternad, P. Gollob, V. Hennige, M. Wilkening, Chem. Mater. 27 (2015) 1740–1750.
[42] A. Dunst, M. Sternad, V. Epp, M. Wilkening, J. Phys. Chem. C 119 (2015) 12183–12192.
[43] M. Murakami, K. Shimoda, S. Shiotani, A. Mitsui, K. Ohara, Y. Onodera, H. Arai, Y. Uchimoto, Z. Ogumi, J. Phys. Chem. C 119 (2015) 24248–24254.
[44] A. Abragam, Principles of Nuclear Magnetism, Oxford University Press, Oxford, U.K, 1961.
[45] A. Moradabadi, P. Kaghazchi, Appl. Phys. Lett. 108 (2016) 213906.